

3D Microstructured Inorganic Perovskite Materials for Thermal Neutron Detection

Jesus A. Caraveo-Frescas*, Martin G. Reyes-Banda, Leunam Fernandez-Izquierdo, Manuel A. Quevedo-Lopez

Dr. J. A. Caraveo-Frescas*, Dr. M. G. Reyes-Banda, Dr. L. Fernandez-Izquierdo, Prof. M. Quevedo-Lopez

Department of Material Science & Engineering

The University of Texas at Dallas

800 W Campbell Rd Richardson, TX. 75080

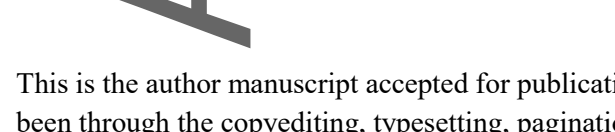
Tel.: +1 972 883 5714; Fax: +1 972 883 5725.

E-mail address: alfonso.caraveo@utdallas.edu

Keywords: Perovskites, Etching, Neutron Detection, Monte-Carlo Simulations

A combination of novel techniques such as a solvent-free thin-film deposition, perovskite patterning, and ¹⁰B back-fill technique enabled the high neutron detection efficiency in a perovskite-based microstructured thermal neutron detector. High-efficiency cesium lead bromide (CsPbBr₃) perovskite-based micro-structured detectors are demonstrated in this work. Trenches up to 10 µm deep were etched into the CsPbBr₃ thin films using a novel dry etching process involving a combination of HBr and Ar plasma. The micro-structured diodes were then backfilled with isotopically enriched Boron as neutron conversion material via a sedimentation process to preserve the perovskite integrity. The fabricated micro-structured CsPbBr₃ thermal neutron detectors show an efficiency of 4.3%. This represents >1.2x efficiency improvement over planar silicon (3.5%) and >2x efficiency improvement over planar CsPbBr₃ (2.1%) detectors, respectively. More importantly, gamma-ray discrimination of 10⁷ was measured in CsPbBr₃-based microstructured neutron detectors.

1. Introduction



This is the author manuscript accepted for publication and has undergone full peer review but has not been through the copyediting, typesetting, pagination and proofreading process, which may lead to differences between this version and the <u>Version of Record</u>. Please cite this article as <u>doi:</u> 10.1002/admt.202100956.

Hybrid lead halide perovskites with a chemical formula of APbX₃, where A is an organic cation and X is CI, Br, or I, have emerged as alternative semiconductors for photovoltaic (PV) devices ^[1]. These perovskites materials have also gained attention for other radiation-related applications^[2,3] where the stability of hybrid perovskites under ambient conditions is poor^[4,5]. Among several perovskites, CsPbX₃ (X=CI, Br, I), has gained more attention not only because it possesses excellent electric, electronic and spectroscopic properties^[6–16] but also because its endurance to humidity and temperature as it lacks organic molecules^[17,18]. It also showed good stability under extreme test conditions^[15], making it an ideal material for high-energy radiation detectors^[13,19,20].

The need of radiation detectors with high efficiency and wide-area coverage is of high importance in applications such as nuclear medicine, industrial imagining, environmental radioactivity monitoring, spacecraft applications, and homeland security^[3,6,19]. For these applications, the detector material should be capable of strongly interact with high-energy particles, must withstand operation at high electric fields with negligible leakage current, possess high resistivity, and be industrially scalable with low-cost production^[17].

CsPbBr₃ is a direct bandgap (2.3 eV) semiconductor with large diffusion lengths and high carrier mobility^[7], and excellent tolerance to structural defects when compared to other semiconductor materials^[21]. This material maintains its semiconducting properties even when a large number of defects (point defects, dislocations, grain boundaries, etc.) are present. Nonetheless, as in any other semiconductor, a high defect density negatively impacts device performance by limiting carrier mobility, life-time, and reliability^[22]. In particular, charge collection efficiency decreases due to increased charge recombination caused by these defects^[23]. For example, neutron detection efficiency of detectors is significantly reduced due to poor charge collection^[24]. High defect tolerance of CsPbBr₃ perovskite positively impacts the radiation hardness of neutron detectors based on this material^[25,26].

Commercially available radiation sensing materials such as CdZnTe (CZT) have been in continuous development as γ -ray detectors since the 1970s, but it still has unresolved issues such as This article is protected by copyright. All rights reserved.

nonuniform response due its inhomogeneity in composition. Furthermore, its high cost limits widespread use^[17]. In comparison, CsPbBr₃ along with low-cost, tunable stoichiometry and stability possesses larger effective atomic number ($Z_{eff} = 65.9$) than CZT ($Z_{eff} = 50.2$)^[17]. Thus, the attenuation coefficient for γ -rays of CsPbBr₃ is higher than CZT^[19]. So far, CsPbBr₃ detectors have shown energy resolving capability under both X and γ -rays, achieving 3.9% (4.8 keV, FWHM) energy resolution for 122 keV ⁵⁷Co γ -ray^[3,17] and more recently, 1.4% was achieved by a small single crystal for 662 keV ¹³⁷Cs γ -ray^[27]. Besides X- and γ -rays, the quantitative detection of charged particles (α , β) is also important as they occur in numerous nuclear decay and nuclear reactions^[3]. The reported use of CsPbBr₃ for heavily charged particle sensing is limited to single crystals grown by methods such as anti-solvent method (AVC)^[11], Bridgman growth method^[28], and inverse temperature crystallization method (ITC) using Shottly diodes fabricated by depositing metals on the front and backside of the crystal^[28,29].

Alpha particle detection was recently reported using CsPbBr₃ single crystals with hole and electron mobilities of 49 and 63 cm²/Vs, respectively, resulting in an energy resolution of 15% for 5.5 MeV alpha particles^[3]. These results indicate that CsPbBr₃ possesses excellent charge transport properties and great potential to be used as thermal neutron detectors if properly coupled with a neutron conversion layer. Nevertheless, the large thickness (~1mm) of single-crystal detectors is a potential issue as it makes the system highly sensitive to gammas. The perovskite single-crystal diode requires high operating voltage (>100 V), limiting its portability. To overcome these issues, the thickness of CsPbBr₃ crystal must be significantly reduced. However, it becomes increasingly difficult to grow and handle such small thicknesses (<100 μm) of single crystals. Therefore, one alternative is to use CsPbBr₃ thin-films. Despite the easy deposition and low-cost that the solution-process offer, perovskite films are not only more susceptible to degradation but also are limited in thickness because several cycles are needed to achieve films with thickness above 1 μm. To challenge such limitations, close spaced sublimation (CSS) method was recently proposed as an alternative to grow stoichiometric films with controllable thickness from sublimated CsPbBr₃ crystals^[30]; Moreover, CSS allows to modulate film

composition trough an ion-exchange recrystallization treatment that results in a enhancement of their transport characteristics^[31]. The resulting planar thin-film CsPbBr₃/Ga₂O₃-based, p-n junction diodes, coupled with ¹⁰B neutron conversion film, have been demonstrated previously by our group showing a thermal neutron detection efficiency of 2.5%^[30] with low voltage operation and high gamma discrimination. Our simulation results show that the theoretical thermal neutron detection efficiency of planar detectors coupled with a ¹⁰B conversion layer is limited to ~4.5%. This is due to the self-absorption of reaction products within the neutron conversion layer^[32]. To achieve higher efficiencies, micro-structured silicon diodes, backfilled with a neutron conversion material, have been demonstrated silicon diodes, backfilled with a neutron conversion material, have been demonstrated silicon fruit probability. Semiconductor patterning greatly increases surface area, thus increasing neutron capture probability Furthermore, thin-film-based microstructured detectors can be scaled for large-area applications. Such scalability would be extremely difficult when using single-crystal semiconductors.

In this paper, we built upon our previously reported thin-film planar detectors to demonstrate high thermal neutron detection efficiency using micro-structured thin-film CsPbBr₃-based diodes^[30]. We patterned trenches of up to 10 μm deep into the CsPbBr₃ layer via a HBr and Ar plasma dry etching process to then-backfill them with ¹⁰B using a sedimentation process designed to prevent any damage to the perovskite layer. The fabricated microstructured CsPbBr₃ thermal neutron detectors show a detection efficiency of 4.3%. This represents >1.2x efficiency improvement over planar silicon (3.5%) and >2x efficiency improvement over planar CsPbBr₃ (2.1%) detectors, respectively. Given the much lower thickness of our thin-film detectors (13 μm), gamma-ray discrimination of 10⁷ was measured in CsPbBr₃-based microstructured neutron detectors.

2. CsPbBr₃ Thin Film Deposition and Etching

Figure 1(a) shows a schematic of CsPbBr₃-based planar neutron detectors. The planar diodes were fabricated by depositing a 13 μm thick p-type CsPbBr₃ thin film by Closed Space Sublimation (CSS) on a 120 nm thick n-type sputtered Ga₂O₃ thin film. ITO and Au were used as bottom and top electrodes and isotopically enriched boron (¹⁰B) was used as a neutron conversion layer. A lead chloride (PbCl₂) treatment was performed on the as-deposited perovskite layer to promote crystal growth and This article is protected by copyright. All rights reserved.

improve the electrical properties; additionally, such treatment results in a Cl containing perovskite with the formula CsPbBr_{3-x}Cl_x^[31] herein referred as CsPbBr₃ film. The detailed experimental methods for the fabrication of planar CsPbBr₃-based detectors are reported elsewhere^[30]. Figure 1(b) shows the schematic cross-section of microstructured CsPbBr₃-based detectors used in this work to increase detection efficiency.

A dry etch process was developed to enable microstructuring of CsPbBr₃. Figure 1(c) shows the etching rate for CsPbBr₃ films using different gases. The inset is a SEM image of the achieved microstructure in CsPbBr₃ film. The HBr+Ar mixture shows the highest etching rate (\sim 230 nm/min) while using HBr alone shows a slightly lower etch rate (200 nm/min). The BCl₃+Cl₂+Ar, HBr+Cl₂, and pure Argon, showed significantly lower etch rates and were not considered for further analysis. The slower etch rate in pure HBr plasma can be attributed to the slow formation rate of ions in the reaction HBr + $e \rightarrow H^+ + Br^- + e$ during the plasma etching.

Similarly, a quick decay of H⁺ and Br⁻ ions due to the interaction with molecular HBr or Br₂ species in the plasma results in slow perovskite etching rate when using pure HBr plasma^[36]. On the other hand, the addition of Ar to HBr enhances the dissociation of H⁺ and Br⁻ ions in the plasma by delaying the decay of these ions^[37]. The presence of Ar ions in the plasma also increases the removal by physically sputtering the perovskite. Therefore, the enhanced presence of dissociated ions and physical sputtering results in the higher etching rate observed in HBr+Ar mixture. Nonetheless, excess of Ar decreases the number of reactive H⁺ and Br⁻ species in the plasma, slowing the etch rate. Figure 1(d) shows the effect of Ar content in the HBr + Ar mixture on the etch rate of CsPbBr₃ films. The maximum etch rate is observed at 20% Ar content, as increasing Ar content results in dilution of reactive ion species in the plasma leading to a decrease in etch rate. 20% Ar content in HBr + Ar mixture was found to be the optimal value to etch microstructures in CsPbBr₃ thin films. The inset of Figure 1(c) shows a SEM image of the microstructures achieved using the optimized mixture.

The proposed etch mechanism of CsPbBr3 using HBr+Ar plasma can be written as:

$$CsPbBr_{3(s)} + 4 HBr_{(g)} \rightarrow CsBr_{(g)} + PbH_{4(g)} + 6 Br_{(g)}^{-}$$
 (1)

HBr produces H⁺ and Br⁻ species which acts as the primary etching species forming volatile cesium bromide (CsBr) and lead tetrahydride (PbH₄), which are easily removed from the etching chamber. The microstructure patterning process is discussed in detail in the Experimental Methods section.

3. Monte-Carlo Simulations of Micro-structured CsPbBr₃-based Detectors

After a successful CsPbBr₃ film patterning demonstration, and once we identified our experimental limitations, thermal neutron detection efficiency for microstructured CsPbBr₃ diodes was theoretically calculated. The neutron detection efficiencies of microstructured CsPbBr₃-based detectors can be increased not only by increasing the depth of microstructure but also by controlling the microstructure geometry. Monte-Carlo nuclear particle code (MCNP) program was used to simulate the neutron detection efficiency of microstructured detectors with varying trench depths from 0 μm (planar diode) to 60 μm and varying trench spacing from 3 μm to 7 μm, while keeping the trench top opening at 5 μm and 4 μm at the bottom, as depicted in the inset of Figure 2. The choice of trench dimensions was based on our experimental observations, as we could not achieve trenches below 5 μm spacing. For the simulations, a density of 4.56 g/cm³ and 2.32 g/cm³ was set for CsPbBr₃ and ¹⁰B, respectively.

As shown in Figure 2, neutron detection efficiency increases when increasing trench depth and reducing trench spacing. When the detector has a higher density (smaller spacing) of deeper trenches, the neutron interaction probability increases due to the larger interaction area. Neutron detection efficiency of 35% in CsPbBr₃ diodes can be obtained with structures as deep as 60 μm and 3 μm spacing while dropping to 23% when using a 7 μm spacing at the same depth. The increase in neutron detection efficiency is due to increased neutron interaction probability from 10% in planar diodes (0 μm) to 98% in microstructured sensors^[35]. Neutron detection efficiency decreases with increasing spacing between microstructures, which is a result of self-absorption of alpha particles by the ¹⁰B neutron conversion layer^[38] that fills the microstructures. Therefore, smaller trench geometries with high-aspect-ratios are preferred to enable high neutron detection efficiency.

4. CsPbBr₃/Ga₂O₃ Diode Fabrication and Characterization

To demonstrate thermal neutron detection, p-n junction diodes with a p-type microstructured CsPbBr₃ film (13 µm thick) and an n-type Ga₂O₃ film (120 nm) and ITO and Au bottom and top electrodes, respectively, were fabricated as described in the experimental section. Trenches of 6 µm, 8 um, and 10 μm depth and ~5 μm spacing were patterned into the 13 μm thick CsPbBr₃ layer to compare both the electrical characteristics as well as the thermal neutron detection efficiency with the planar diode. The resulting I-V diode characteristics are shown in Figure 3(a), where all devices show good rectification characteristics. It is evident that the leakage current increases as a function of microstructure depth, from $\sim 4 \times 10^{-9}$ A for the planar device (13 µm) to $\sim 4 \times 10^{-8}$ A for the 10 µm deep microstructured device (Figure 3b). This results from the generation of surface states at the side-walls of microstructures due to defects created during etching. These surface states negatively impact the electrical performance of the CsPbBr₃ detectors by compromising charge collection. The recombination is more likely to occur at the metal-semiconductor interface, which is enhanced due to the presence of interfacial defects^[39]. The side-wall etch damage significantly impacts the ability of the diodes to transport the carriers generated in the depletion region without recombining. The increasing leakage current of the diodes and recombination at the side-walls cause a decrease in charge collection efficiency of the detector diodes. Figure 3b shows both the leakage current and charge collection efficiency of the studied diodes. Increasing trench depth generates more surface defects that increase the diode leakage current and decreases charge collection efficiency. For neutron detection, the diodes are used in the reverse bias region; hence the increase in leakage current as a function of trench depth negatively influences detection efficiency. Future experiments should focus on ways to passivate surface defects and/or heal the damaged CsPbBr₃ patterned surface so that the leakage current of microstructured diodes is closer to the one observed in planar devices.

The microstructured diodes were successfully filled with the thermal neutron conversion material ¹⁰B via sedimentation process, as shown in Figure 4(a). Negligible differences in the I-V diode characteristics were observed in all devices, confirming no damage to the perovskite layer after ¹⁰B

sedimentation. Despite not achieving 100% trench filling, there is no presence of large voids. This is mainly due to the wide opening of trenches (5 μm) that enabled ¹⁰B particles (~ 100nm average size) to easily back-fill the microstructures. The irregular shape and different sizes of ¹⁰B powder particles enable the close-packed filling. In addition, the inclusion of PVP k-90 in the suspension provides mechanical stability to the back-filled ¹⁰B inside the trenches. However, tiny voids between the ¹⁰B particles prevent microstructures from attaining the desired 100% fill density, as seen in the SEM images of Figure 4(a).

5. Radiation Detection Efficiency of Micro-structured CsPbBr₃/Ga₂O₃ Detectors

Figure 4(b) shows the experimental thermal neutron detection efficiency of CsPbBr₃ based detectors and the theoretical efficiency calculated by MCNP. The experimental and theoretical efficiencies of the planar Si detector are indicated with a star symbol for comparison. As the microstructure depth increases, neutron detection efficiency increases from 2.1% in the planar perovskite-based detector to 4.3% in the device with 10 µm deep microstructures. This efficiency is already higher than the experimental efficiency of planar Si diodes (3.5%), which highlights how promising perovskite-based diodes are for thermal neutron detection. Furthermore, the device stability was evaluated for up to 30 days with no significant change in their performance.

The discrepancy in experimental neutron detection efficiency compared with theoretical efficiency in Figure 4(b) can be attributed to two major reasons: the packing density of ¹⁰B in the microstructures and poor charge collection efficiency in the detectors^[35]. In theoretical calculations, the microstructures were assumed to contain ¹⁰B with 100% filling density, whereas in the experiments, a 100% filling density is unlikely to be achieved. Figure 4(a) shows the SEM cross-sectional images of microstructured CsPbBr₃ diodes back-filled with ¹⁰B powders for the three depths discussed here (6 μm, 8 μm, and 10 μm) where tiny gaps between particles can be seen. On the other hand, it is well-known that the etch process permanently damages the side-walls during trench formation. The surface recombination of charges generated by incident alpha particles (emitted after neutron conversion in the ¹⁰B layer) at the surfaces defects created during dry etching is more pronounced and thus negatively This article is protected by copyright. All rights reserved.

impacts the charge collection efficiency of the diode when used as a thermal neutron detector^[40]. As the etching depth increases, so does the number of surface defects as observed during diode characterization. When the diode is employed as a thermal neutron detector, it is used under reverse bias, so the higher the number of surface states, the higher the diode's leakage current and the lower the detection efficiency. This can be seen in the broadening discrepancy of experimental efficiency as a function of trench depth, where more surface states are present and observed by the increase in the diode leakage current (Figure 3a).

Finally, to demonstrate the γ /n discrimination rate, the microstructured detectors were exposed to Cesium-137 (137 Cs) isotope. As shown in Figure 4(c), the lowest γ /n discrimination of 5.6×10^{-7} was obtained in microstructured CsPbBr₃-based detectors for 1332 keV gamma rays. This confirms the superior γ /n discrimination of thin-film-based micro-structured CsPbBr₃/Ga₂O₃ detectors, which is three orders of magnitude better than the values observed in planar silicon detectors.

6. Conclusions

We have successfully fabricated diodes with the structure ITO/Ga₂O₃/CsPbBr₃/Au using a 13 μm thick CsPbBr₃ layer deposited by CSS and patterned trenches into it with a 5 μm spacing and 6 μm, 8 μm, and 10 μm depth via a dry etching process using HBr+Ar plasma. A sedimentation process was developed to back-fill the microstructures with ¹⁰B neutron conversion material preserving the chemical integrity of microstructured CsPbBr₃ thin films. Microstructured CsPbBr₃ based detectors show a thermal neutron detection efficiency up to 4.3%, which is ~125% of planar silicon detectors. This represents >1.2x efficiency improvement over planar silicon (3.5%) and >2x efficiency improvement over planar CsPbBr₃ (2.1%) detectors, respectively. Given the much lower thickness of our thin-film detectors, gamma-ray discrimination of 10⁷ was measured in CsPbBr₃-based microstructured neutron detectors. The dry etching process created surface defects that negatively impact the diode charge collection efficiency, thus decreasing neutron detection efficiency. Strategies to passivate the surface defects and/or heal the patterned perovskite surface need to be explored to further improve device performance and achieve microstructures with high aspect ratios. Neutron detection efficiency shown This article is protected by copyright. All rights reserved.

in this work is the highest intrinsic efficiency demonstrated in a non-silicon-based device to the best of our knowledge. Overall, CsPbBr₃ and the etch method shown here indicate a great potential to achieve high neutron detection efficiencies comparable with silicon technology. The presence of heavy elements in CsPbBr₃ allows the complete alpha particle absorption at lower thickness than silicon. Furthermore, the deposition method used here is a wide area compatible manufacturing technique that enables the fabrication of neutron detectors over large area (m² scale) at a cost point that would otherwise be prohibitive when using single crystal silicon devices.

7. Experimental Methods

Device simulation. A commercially available 3-D finite element TCAD software package (Silvaco Atlas) was used for the numerical simulations of the planar and microstructured CsPbBr₃ diodes^[41]. The electrical response in the diode part of the detector was studied using this software. Then, the range of alpha particles generated from the 10 B(n, α) 7 Li reaction in the perovskite films was simulated using the stopping and range of ions in matter (SRIM) and the transport of ions in matter (TRIM) software [42]. TRIM was predominantly used to calculate the range of alpha particles in the perovskite portion of the detector [43]. The neutron detection efficiency of the CsPbBr₃ perovskites was simulated using the Monte-Carlo nuclear particle (MCNP) code. The neutron capture ion algorithm (NCIA) was used to study the neutron capture in the 10 B that produces alphas according to the reaction 10 B(n, α) 7 Li. The pulse height fally tool of MCNP was used to determine the charge deposited by the alpha particles in the microstructured diodes $^{[44,45]}$.

Perovskite layer patterning and diode fabrication. The diode fabrication includes pre-pattering commercially available indium doped tin oxide (ITO) on a 2.5 cm × 2.5 cm glass substrate. Patterned ITO determines the active area of the diode (0.79 mm²) while serving as a cathode of the diode. The next step was to deposit a blanket of n-type layer, in this case, 120nm of Ga₂O₃ by reactive sputtering at room temperature. Next, for the p-type thin film layer, CsPbBr₃ crystals grown by the antisolvent vapor-assisted crystallization (AVC) method were used as a source. The crystals were sublimated on top of the Ga₂O₃ layer to deposit 13 μm thick CsPbBr₃ thin films using the close-spaced sublimation This article is protected by copyright. All rights reserved.

(CSS) technique following a solid-state ion-exchange process also done in the CSS chamber, using a PbCl₂ precursor. Finally, Au contacts were deposited by e-beam on top of the perovskite to serve as the anode. The detailed process for the perovskite deposition step was demonstrated elsewhere by our group^[30] as well as the ion-exchange treatment^[31]. A thin layer of metallic chromium was deposited on the perovskite layer to serve as the hard mask for microstructure etching. This layer is designed to be self-sacrificing such that it was completely removed at the end of microstructure etching using the HBr+Ar plasma. The etch rate of Cr in the HBr+Ar plasma was found to be 17 nm/min, therefore 600 nm of Cr was used as a hard mask to etch 8 μm of CsPbBr₃. A 200 nm thick TiN layer was used as a secondary hard mask to transfer the photoresist pattern to the Cr layer. Standard photolithography was used to pattern the photoresist layer that was spin-coated on top of the Cr/TiN hard mask. Then, the TiN layer was etched using a Cl₂ plasma for 220 seconds. The Cr layer was dry-etched using a 4:1 Cl₂ + O₂ plasma. PR was completely removed during this step as the plasma contains Oxygen, as well as the TiN layer due to the presence of Chlorine in the mixture. At the end of the process, we end up with a Cr layer that is going to be used as the hard mask for the perovskite patterning step.

To etch the microstructures into the perovskite layer, plasma-based etching was explored. Several types of gases, including hydrogen bromide (HBr), boron chloride (BCl₃), chlorine (Cl), hydrogen (H), and argon (Ar), were used to identify the best combinations to etch microstructures in CsPbBr₃. The optimized mixture of HBr + Ar was performed using a 4:1 gas ratio at 10 mTorr, 750 W ICP power, and 250 W bias power. The tapering seen in microstructures is mainly due to the limited directionality in the etching process. It can be attributed to the removal of the hard mask along with CsPbBr₃ during etching. Typically, hard mask removal occurs when the physical sputtering component of plasma is strong (in this case presence of Ar in the plasma). The last step of the microstructured diode fabrication process was to deposit gold contacts on the top using a shadow mask that acts as an anode of the diode. For the planar diode fabrication, the hard mask deposition and the etching steps were skipped to directly deposit gold contacts immediately after the perovskite deposition step.

Microstructure back-filling process. To fill the neutron conversion material (¹⁰B powder) in the This article is protected by copyright. All rights reserved.

microstructured CsPbBr₃ diode, a sedimentation technique was implemented. The back-filling process by sedimentation was enabled using boron nanoparticles having an average particle size of 100nm. The process starts with preparing a mixture of boron nanoparticles (27 mg), acetone (7g), isopropyl alcohol (8.7 g), and PVP (9 mg). A suspension is made by dissolving the boron in the solvents using sonication. In the next step, the suspension was dispersed onto a Petri dish with the microstructured CsPbBr₃ device. Then the solvents were allowed to evaporate over 6 hours inside a fume hood to let the boron nanoparticles settle down by gravitation.

Device chalacerization. The current-voltage (I-V) and capacitance-voltage (C-V) characteristics of the diode were measured using Keithley 4200 and Agilent 4284, respectively. The I-V measurement included voltage sweep from -5 V to 5 V and the C-V measurement performed at 100 kHz. Since the detector operates at reverse bias, sweeping to -5V was done to ensure complete depletion of the diode. For radiation measurement, the devices were first tested for alpha particles using Polonium-210 (210Po) with the samples mounted on a printed circuit board (PCB). The detector was placed 1.5 cm away from the 210Po source in a dark aluminum chamber to replicate the 1.4 MeV alphas from the ¹⁰B(n,α)⁷Li reaction. Similarly, for neutron testing using Californium-252 (252Cf), the sample mounted on a PCB was placed in a dark stainless-steel chamber under vacuum. The thermal neutron flux at the measurement position was 9900 thermal neutrons/mm²/h. An Ortec 142A preamplifier was used to apply bias to the diode and pre-amplify the pulse generated by the alphas in the diode. Pulse shaping was done in an Ortec 575 shaping amplifier. An Ortec EASY-MCA-2K multi-channel analyzer was used to measure the pulses/channel. The setup for neutron detection used in this work is shown elsewhere^[21].

Acknowledgment

The authors would like to thank Dr. Siddartha S. Nandagopala Krishnan for conducting the experiments as well as our sponsor, Nanoholdings, for facilitating this research. This work was partially supported by AFOSR Grants FA9550-519 18-1-0019 and NSF/PFI:AIR TT 1701192.

2365709x, 2022, 6, Downloaded from https://onlinelibrary.wiley.com/doi/10.1002/admt.202109956 by Manuel Quevedo-Lopez - University Of Texas - Dallas , Wiley Online Library on [27012025]. See the Terms and Conditions (https://onlinelibrary.wiley.com/terms-and-conditions) on Wiley Online Library for rules of use; OA articles are governed by the applicable Centarive Commons

References

- [1] G. Mannino, I. Deretzis, E. Smecca, A. La Magna, A. Alberti, D. Ceratti, D. Cahen, *J. Phys. Chem. Lett.* **2020**, *11*, 2490.
- [2] L. Pan, Y. Feng, P. Kandlakunta, J. Huang, L. R. Cao, *IEEE Transactions on Nuclear Science* **2020**, 67, 443
- [3] Y. He, Z. Liu, K. M. McCall, W. Lin, D. Y. Chung, B. W. Wessels, M. G. Kanatzidis, *Nuclear Instruments and Methods in Physics Research Section A: Accelerators, Spectrometers, Detectors and Associated Equipment* **2019**, *922*, 217.
- [4] W. Zhu, C. Bao, F. Li, T. Yu, H. Gao, Y. Yi, J. Yang, G. Fu, X. Zhou, Z. Zou, Nano Energy **2016**, *19*, 17.
- [5] G. Náfrádi, E. Horváth, M. Kollár, A. Horváth, P. Andričević, A. Sienkiewicz, L. Forró, B. Náfrádi, Energy Conversion and Management **2020**, *205*, 112423.
- [6] C. C. Stoumpos, C. D. Malliakas, J. A. Peters, Z. Liu, M. Sebastian, J. Im, T. C. Chasapis, A. C. Wibowo, D. Y. Chung, A. J. Freeman, B. W. Wessels, M. G. Kanatzidis, *Crystal Growth & Design* 2013, 13, 2722.
- [7] G. R. Yettapu, D. Talukdar, S. Sarkar, A. Swarnkar, A. Nag, P. Ghosh, P. Mandal, *Nano Lett.* **2016**, 16, 4838.
- [8] X. Li, Y. Wu, S. Zhang, B. Cai, Y. Gu, J. Song, H. Zeng, Advanced Functional Materials 2016, 26, 2584
- [9] J. Ding, S. Du, Z. Zuo, Y. Zhao, H. Cui, X. Zhan, J. Phys. Chem. C 2017, 121, 4917.
- [10] J.-H. Cha, J. H. Han, W. Yin, C. Park, Y. Park, T. K. Ahn, J. H. Cho, D.-Y. Jung, *J. Phys. Chem. Lett.* **2017** *8*, 565.
- [11] Y. Rakita, N. Kedem, S. Gupta, A. Sadhanala, V. Kalchenko, M. L. Böhm, M. Kulbak, R. H. Friend, D. Cahen, G. Hodes, *Crystal Growth & Design* **2016**, *16*, 5717.
- [12] M. I. Saidaminov, M. A. Haque, J. Almutlaq, S. Sarmah, X.-H. Miao, R. Begum, A. A. Zhumekenov, I. Dursun, N. Cho, B. Murali, O. F. Mohammed, T. Wu, O. M. Bakr, *Advanced Optical Materials* **2017**, *5*, 1600704.
- [13] H. Zhang, X. Liu, J. Dong, H. Yu, C. Zhou, B. Zhang, Y. Xu, W. Jie, *Crystal Growth & Design* **2017**, *17*, 6426.
- [14] Z. Shi, L. Lei, Y. Li, F. Zhang, Z. Ma, X. Li, D. Wu, T. Xu, Y. Tian, B. Zhang, Z. Yao, G. Du, *ACS Appl. Mater. Interfaces* **2018**, *10*, 32289.
- [15] Y. Zhang, R. Sun, X. Ou, K. Fu, Q. Chen, Y. Ding, L.-J. Xu, L. Liu, Y. Han, A. V. Malko, X. Liu, H. Yang, O. M. Bakr, H. Liu, O. F. Mohammed, ACS Nano 2019, 13, 2520.

2365709x, 2022, 6, Downloaded from https://onlinelibrary.wiley.com/doi/10.1002/admt.202100956 by Manuel Quevedo-Lopez - University Of Texas - Dallas , Wiley Online Library on [27012025]. See the Terms and Conditions (https://onlinelibrary.wiley.com/terms-and-conditions) on Wiley Online Library on [27012025].

- [16] Z. Liu, J. A. Peters, C. C. Stoumpos, M. Sebastian, B. W. Wessels, J. Im, A. J. Freeman, M. G. Kanatzidis, in *Hard X-Ray, Gamma-Ray, and Neutron Detector Physics XV*, International Society For Optics And Photonics, 2013, p. 88520A.
- [17] Y. He, L. Matei, H. J. Jung, K. M. McCall, M. Chen, C. C. Stoumpos, Z. Liu, J. A. Peters, D. Y. Chung, B. W. Wessels, M. R. Wasielewski, V. P. Dravid, A. Burger, M. G. Kanatzidis, *Nat Commun* 2018, 9, 1609.
- [18] W. Chen, J. Zhang, G. Xu, R. Xue, Y. Li, Y. Zhou, J. Hou, Y. Li, *Advanced Materials* **2018**, *30*, 1800855.
- [19] J. H. Heo, D. H. Shin, J. K. Park, D. H. Kim, S. J. Lee, S. H. Im, *Advanced Materials* **2018**, *30*, 1801743.
- [20] Q. Chen, J. Wu, X. Ou, B. Huang, J. Almutlaq, A. A. Zhumekenov, X. Guan, S. Han, L. Liang, Z. Yi, J. Li, X. Xie, Y. Wang, Y. Li, D. Fan, D. B. L. Teh, A. H. All, O. F. Mohammed, O. M. Bakr, T. Wu, M. Bettinelli, H. Yang, W. Huang, X. Liu, *Nature* **2018**, *561*, 88.
- [21] J. Kang, L.-W. Wang, J. Phys. Chem. Lett. 2017, 8, 489.
- [22] Y. Kang, S. Han, Phys. Rev. Applied 2018, 10, 044013.
- [23] M. Bruzzi, F. Gabelloni, N. Calisi, S. Caporali, A. Vinattieri, Nanomaterials 2019, 9, 177.
- [24] L. Smith, J. W. Murphy, J. Kim, S. Rozhdestvenskyy, I. Mejia, H. Park, D. R. Allee, M. Quevedo-Lopez, B. Gnade, *Nuclear Instruments and Methods in Physics Research Section A: Accelerators, Spectrometers, Detectors and Associated Equipment* **2016**, *838*, 117.
- [25] F. Lang, O. Shargaieva, V. V. Brus, H. C. Neitzert, J. Rappich, N. H. Nickel, *Advanced Materials* **2018**, *30*, 1702905.
- [26] M. Ahmad, G. Rehman, L. Ali, M. Shafiq, R. Iqbal, R. Ahmad, T. Khan, S. Jalali-Asadabadi, M. Maqbool, I. Ahmad, *Journal of Alloys and Compounds* **2017**, *705*, 828.
- [27] Y. He, M. Petryk, Z. Liu, D. G. Chica, I. Hadar, C. Leak, W. Ke, I. Spanopoulos, W. Lin, D. Y. Chung, B. W. Wessels, Z. He, M. G. Kanatzidis, *Nature Photonics* **2021**, *15*, 36.
- [28] P. Zhang, Q. Sun, Y. Xu, X. Li, L. Liu, G. Zhang, X. Tao, Crystal Growth & Design 2020, 20, 2424.
- [29] H. Wei, J. Huang, Nature Communications **2019**, *10*, 1066.
- [30] L. Fernandez-Izquierdo, M. G. Reyes-Banda, X. Mathew, I. R. Chavez-Urbiola, L. E. Bouanani, J. Chang, C. Avila-Avendano, N. R. Mathews, M. I. Pintor-Monroy, M. Quevedo-Lopez, *Advanced Materials Technologies* **n.d.**, *n/a*, 2000534.
- [31] M. G. Reyes Banda, L. Fernandez-Izquierdo, S. S. Nandagopala Krishnan, J. A. Caraveo-Frescas, X. Mathew, M. Quevedo-López, *ACS Appl. Electron. Mater.* **2021**, DOI 10.1021/acsaelm.1c00072.

2365709x, 2022, 6, Downloaded from https://onlinelibrary.wiley.com/doi/10.1002/admt.202100956 by Manuel Quevedo-Lopez - University Of Texas - Dallas, Wiley Online Library on [27/01/2025]. See the Terms and Conditions (https://onlinelibrary.wiley.com/doi/10.1002/admt.202100956 by Manuel Quevedo-Lopez - University Of Texas - Dallas, Wiley Online Library on [27/01/2025]. See the Terms and Conditions (https://onlinelibrary.wiley.com/doi/10.1002/admt.202100956 by Manuel Quevedo-Lopez - University Of Texas - Dallas, Wiley Online Library on [27/01/2025]. See the Terms and Conditions (https://onlinelibrary.wiley.com/doi/10.1002/admt.202100956 by Manuel Quevedo-Lopez - University Of Texas - Dallas, Wiley Online Library on [27/01/2025]. See the Terms and Conditions (https://onlinelibrary.wiley.com/doi/10.1002/admt.202100956 by Manuel Quevedo-Lopez - University Of Texas - Dallas, Wiley Online Library on [27/01/2025]. See the Terms and Conditions (https://onlinelibrary.wiley.com/doi/10.1002/admt.202100956 by Manuel Quevedo-Lopez - University Of Texas - Dallas, Wiley Online Library on [27/01/2025]. See the Terms and Conditions (https://onlinelibrary.wiley.com/doi/10.1002/admt.202100956 by Manuel Quevedo-Lopez - University Of Texas - Dallas, Wiley Online Library on [27/01/2025]. See the Terms and Conditions (https://onlinelibrary.wiley.com/doi/10.1002/admt.202100956 by Manuel Quevedo-Lopez - University Of Texas - Dallas, Wiley Online Library on [27/01/2025]. See the Terms and Conditions (https://onlinelibrary.wiley.com/doi/10.1002/admt.202100956 by Manuel Quevedo-Lopez - University Of Texas - Dallas, Wiley Online Library on [27/01/2025]. See the Terms and Conditions (https://onlinelibrary.wiley.com/doi/10.1002/admt.202100956 by Manuel Quevedo-Lopez - University Of Texas - Dallas, Wiley Online Library on [27/01/2025]. See the Terms and Conditions (https://onlinelibrary.wiley.com/doi/10.1002/admt.202100956 by Manuel Quevedo-Lopez - University Of Texas - Dallas, Wiley Online Library on [27/01/2025]. See the Terms and Conditions

- [32] D. S. McGregor, R. T. Klann, H. K. Gersch, E. Ariesanti, J. D. Sanders, B. VanDerElzen, *IEEE Transactions on Nuclear Science* **2002**, *49*, 1999.
- [33] S. L. Bellinger, R. G. Fronk, W. J. McNeil, T. J. Sobering, D. S. McGregor, *Nuclear Instruments and Methods in Physics Research Section A: Accelerators, Spectrometers, Detectors and Associated Equipment* **2011**, 652, 387.
- [34] R. G. Fronk, S. L. Bellinger, L. C. Henson, D. E. Huddleston, T. R. Ochs, M. A. Reichenberger, C. J. Rietcheck, C. T. Smith, T. J. Sobering, J. K. Shultis, D. S. McGregor, in *2015 IEEE Nuclear Science Symposium and Medical Imaging Conference (NSS/MIC)*, **2015**, pp. 1–5.
- [35] S. S. Nandago pala Krishnan, C. Avila-Avendano, Z. Shamsi, J. A. Caraveo-Frescas, M. A. Quevedo-Lopez, *ACS Sens.* **2020**, *5*, 2852.
- [36] A. Efremov, S. Kang, K.-H. Kwon, W. Seok Choi, *Journal of Vacuum Science & Technology A* **2011**, 29, 06B103.
- [37] L. Jiang, R. Cheung, Microelectronic Engineering 2004, 73–74, 306.
- [38] J. W. Murphy, G. R. Kunnen, I. Mejia, M. A. Quevedo-Lopez, D. Allee, B. Gnade, *Appl. Phys. Lett.* **2012**, *101*, 143506.
- [39] R. Kumar, J. Kumar, P. Srivastava, D. Moghe, D. Kabra, M. Bag, ACS Appl. Mater. Interfaces 2020, 12, 34265.
- [40] G. Wright, Y. Cui, U. N. Roy, C. Barnett, K. Reed, A. Burger, F. Lu, L. Li, R. B. James, *IEEE Transactions on Nuclear Science* **2002**, *49*, 2521.
- [41] SILVACO International Inc., ATLAS User's Manual 2007.
- [42] J. F. Ziegler, J. P. Biersack, 2008.
- [43] J. F. Ziegler, J. P. Biersack, U. Littmark, Pergamon 1985.
- [44] C. J. Werner, J. S. Bull, C. J. Solomon, F. B. Brown, G. W. McKinney, M. E. Rising, D. A. Dixon, R. L. Martz, H. G. Hughes, L. J. Cox, A. J. Zukaitis, J. C. Armstrong, R. A. Forster, L. Casswell, *MCNP Version 6.2 Release Notes*, Los Alamos National Lab. (LANL), Los Alamos, NM (United States), **2018**.
- [45] C. J. Werner, Los Alamos National Laboratory, LA-UR-17-29981 2017.



2367/98s, 2022. 6, Downloaded from https://onlinelibrary.wiley.com/doi/10.1002/admt.202100956 by Manuel Quevedo-Lopez - University Of Texas - Dallas , Wiley Online Library or rules of use; OA articles are governed by the applicable Creative Commons Licenses

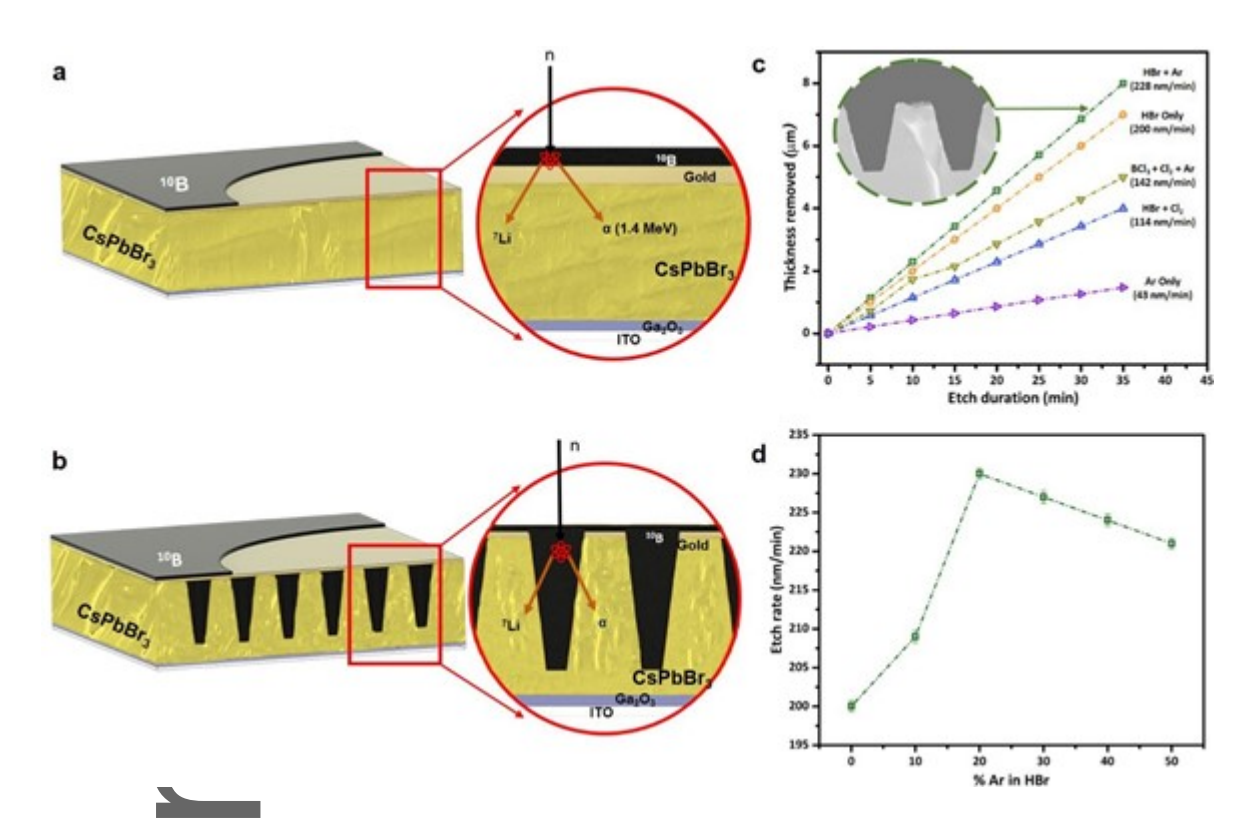


Figure 1: (a) Schematic image of planar CsPbBr₃/Ga₂O₃ neutron detector, (b) Schematic image of micro-structured CsPbBr₃/Ga₂O₃ neutron detector back-filled with ¹⁰B, (c) Etch rate of CsPbBr₃ perovskite in various plasma, and (d) Effect of Ar addition to the HBr on etch rate of CsPbBr₃.

Author

2367/09s, 2022, 6, Downloaded from https://onlinelibrary.wiley.com/doi/10.1002/admt.202100956 by Manuel Quevedo-Lopez - University Of Texas - Dallas , Wiley Online Library on [27/01/2025]. See the Terms and Conditions (https://onlinelibrary.wiley.com/doi/10.1002/admt.202100956 by Manuel Quevedo-Lopez - University Of Texas - Dallas , Wiley Online Library on [27/01/2025]. See the Terms and Conditions (https://onlinelibrary.wiley.com/doi/10.1002/admt.202100956 by Manuel Quevedo-Lopez - University Of Texas - Dallas , Wiley Online Library on [27/01/2025]. See the Terms and Conditions (https://onlinelibrary.wiley.com/doi/10.1002/admt.202100956 by Manuel Quevedo-Lopez - University Of Texas - Dallas , Wiley Online Library on [27/01/2025]. See the Terms and Conditions (https://onlinelibrary.wiley.com/doi/10.1002/admt.202100956 by Manuel Quevedo-Lopez - University Of Texas - Dallas , Wiley Online Library on [27/01/2025]. See the Terms and Conditions (https://onlinelibrary.wiley.com/doi/10.1002/admt.202100956 by Manuel Quevedo-Lopez - University Of Texas - Dallas , Wiley Online Library on [27/01/2025]. See the Terms and Conditions (https://onlinelibrary.wiley.com/doi/10.1002/admt.202100956 by Manuel Quevedo-Lopez - University Of Texas - Dallas , Wiley Online Library on [27/01/2025]. See the Terms and Conditions (https://onlinelibrary.wiley.com/doi/10.1002/admt.202100956 by Manuel Quevedo-Lopez - University Of Texas -

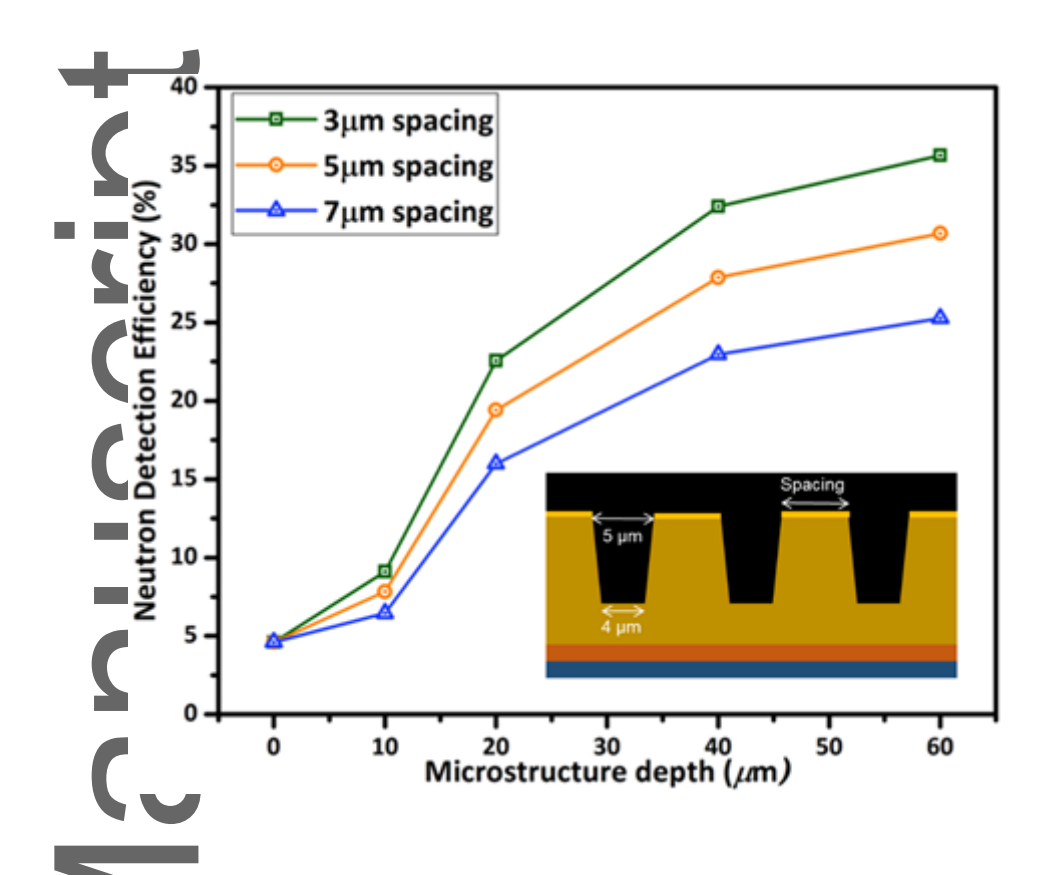
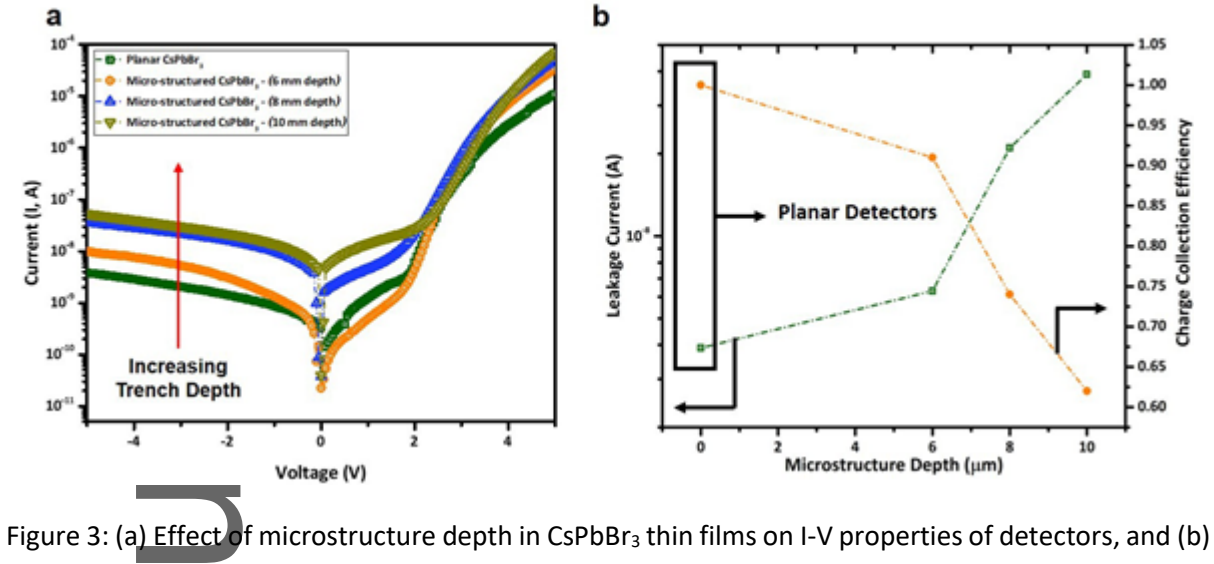


Figure 2: MCNP simulations showing the maximum expected efficiencies using microstructured CsPbBr₃-based detectors.



2367/98s, 2022. 6, Downloaded from https://onlinelibrary.wiley.com/doi/10.1002/admt.202100956 by Manuel Quevedo-Lopez - University Of Texas - Dallas , Wiley Online Library or rules of use; OA articles are governed by the applicable Creative Commons Licenses



The effect of increasing microstructure depth in CsPbBr₃ films on leakage current and charge collection efficiency.

2365709x, 2022. 6, Downloaded from https://onlinelibrary.wiley.com/doi/10.1002/admt.202100956 by Manuel Quevedo-Lopez - University Of Texas - Dallas , Wiley Online Library on [27/01/2025]. See the Terms and Conditions (https://onlinelibrary.wiley.com/derms)

and-conditions) on Wiley Online Library for rules of use; OA articles are governed by the applicable Creative Commons

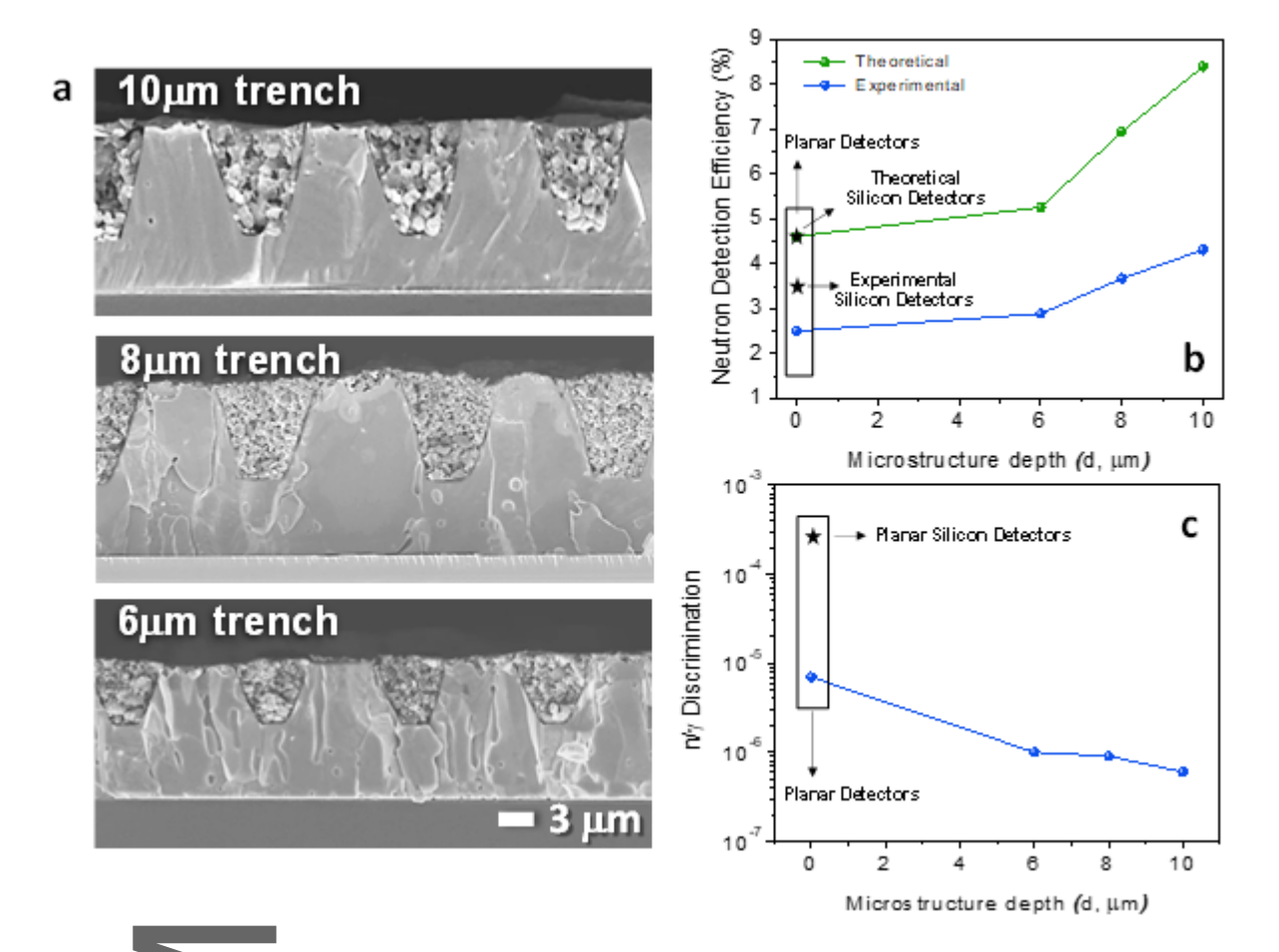
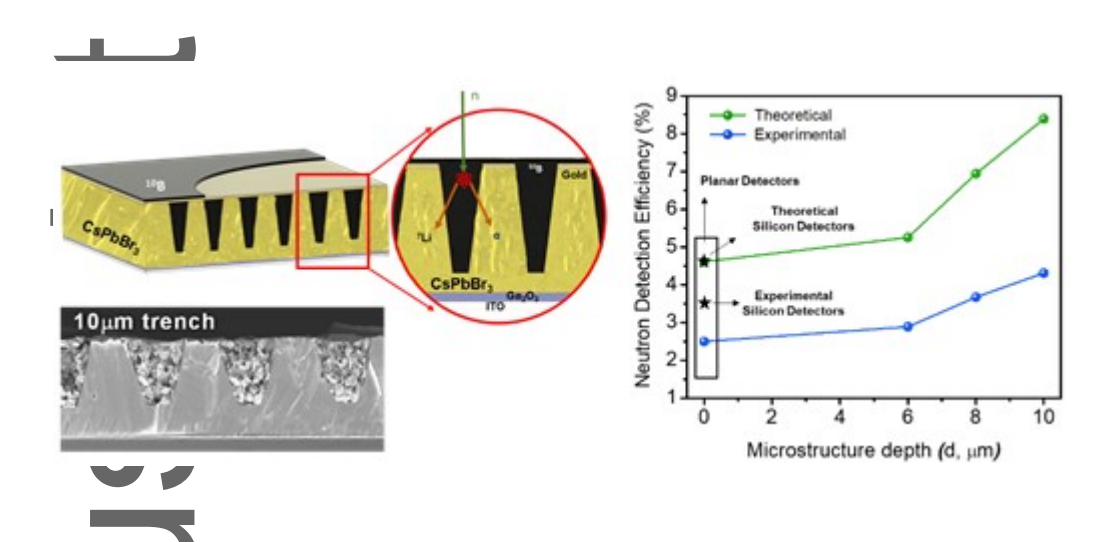


Figure 4: (a) SFM-cross-sectional image of etched microstructures in CsPbBr $_3$ thin films filled with 10 B conversion film, (b) Comparison of neutron detection efficiencies between theoretical simulations and experimental results (the efficiency of planar silicon is represented using star symbol), and (c) Comparison of γ /n discrimination of planar and micro-structured CsPbBr $_3$ /Ga $_2$ O $_3$ detectors (the γ /n discrimination of planar silicon is represented using star symbol).



2365709x, 2022, 6, Downloaded from https://onlinelibrary.wiley.com/doi/10.1002/admt.202100956 by Manuel Quevedo-Lopez - University Of Texas - Dallas , Wiley Online Library on [27/01/2025]. See the Terms and Conditions (https://onlinelibrary.wiley.com/terms

and-conditions) on Wiley Online Library for rules of use; OA articles are governed by the applicable Creative Commons Licensu



High neutron detection efficiency is achieved in microstrutured perovskite-based devices. 10 μ m deep trenches are patterned into a CsPbBr₃ thin film using a dry etching technique and back-filled with isotopically enriched boron particles resulting in intrinsic detection efficiency of 4.3% and excellent gamma ray rejection, superior to planar Silicon based detectors.